Cognitive Neurodynamics
https://doi.org/10.1007/s11571-024-10089-x

RESEARCH ARTICLE

Adult neurogenesis in the hippocampal dentate gyrus affects sparsely synchronized rhythms, associated with pattern separation and integration

Sang-Yoon Kim[1] · Woochang Lim[1]

Received: 1 February 2024 / Revised: 1 February 2024 / Accepted: 14 February 2024

Abstract
We are concerned about sparsely synchronized rhythms (SSRs), associated with diverse cognitive functions, in the hippocampal dentate gyrus. Distinctly, adult-born immature GCs (imGCs) emerge through neurogenesis, in addition to the mature granule cells (mGCs) (emerged in the developmental stage). In prior work, these mGCs and imGCs were found to exhibit their distinct roles in pattern separation and integration for encoding cortical inputs, respectively. But, the underlying dynamical mechanismremains unclear. In this paper, we first study influence of the young adult-born imGCs on emergence of SSRs in the populations of the mGCs and the imGCs; population and individual firing behaviors in the SSRs are intensively studied. We then examine how the SSRs play a role in the underlying mechanism for pattern separation and integration. Particularly, quantitative relationship between SSRs of the mGCs and the imGCs and their pattern separation and integration is investigated.

Keywords Dentate gyrus · Immature granule cells (GCs) · Mature GCs · Sparsely synchronized rhythm

Introduction

The hippocampus, consisting of the dentate gyrus (DG) and the subareas CA3 and CA1, performs significant functions in memory process (Squire 1987; Gluck and Myers 2001). In this paper, our main concern is the DG (corresponding to the gate to the hippocampus). The entorhinal cortex (EC) make excitatory project to the main encoding granule cells (GCs) in the DG through the perforant paths (PPs). Then, the principal GCs make pattern separation (i.e., a process of transforming similar input patterns into less similar output patterns) for effective encoding of the cortical inputs (Marr 1971; McNaughton and Morris 1987; Rolls 1989a, b, c; Willshaw and Buckingham 1990; Treves and Rolls 1991, 1992, 1994; O'Reilly and McClelland 1994; Beck et al. 2000; Nitz and McNaughton 2004; Leutgeb et al. 2007; Bakker et al. 2008; Myers and Scharfman 2009, 2011; Yassa and Stark 2011; Schmidt et al. 2012; Myers et al. 2013; Santoro 2013; Yim et al. 2015; Knierim and Neunuebel 2016; Scharfman and Myers 2016; Rolls 2016; Chavlis et al. 2017; Kassab and Alexandre 2018; van Dijk and Fenton 2018; Kim and Lim 2022b).

Most distinctly, adult neurogenesis occurs in the DG, which leads to appearance of new young immature GCs (imGCs). Pioneering works of Altman for the adult neurogenesis were made several decades ago (Altman 1962, 1963; Altman and Das 1965). Since pioneering works of Altman, young imGCs have been found to emerge via adult neurogenesis in the subgranular zone of the DG (Ming and Song 2011; Spalding et al. 2013; Bayer 2016; Boldrini et al. 2018; Gage 2019; Christian et al. 2020; Wang et al. 2020). The newly-born imGCs move into the granular layer of the DG. They are found to exhibit distinct competing properties such as high excitability, weak inhibition, and low excitatory innervation in contrast to the mature GCs (mGCs) (emerged in the developmental stage) (Aimone et al. 2009, 2011; Sahay et al. 2011a, b; Dieni et al. 2016).

✉ Woochang Lim
wclim@icn.re.kr

Sang-Yoon Kim
sykim@icn.re.kr

[1] Institute for Computational Neuroscience and Department of Science Education, Daegu National University of Education, Daegu 42411, Korea

Here, we consider a spiking neural network for the adult neurogenesis in the DG, composed of both mGCs and imGCs, which was developed in our prior work for the effect of adult-born imGCs on pattern separation (Kim and Lim 2023). In our DG network, both high excitability and low excitatory innervation for the imGCs are considered. We note that the influence of low excitatory innervation (decreasing activation degree) for the imGCs counteracts the influence of their high excitability (increasing activation degree).

Our prior work has shown that the mGCs exhibit pattern separation, while the imGCs show pattern integration (associating dissimilar patterns) (Kim and Lim 2022b, 2023). As shown there, the pattern separation (integration) efficacy of the mGCs (imGCs) becomes better for similar (dissimilar) input patterns. Thus, in a heterogeneous population of mGCs and imGCs, the memory storage capacity in the CA3 could be optimized via cooperative interplay through pattern separation and pattern integration. However, the underlying dynamical mechanism for pattern separation and integration remains unclear.

In this paper, we are concerned about sparsely synchronized rhythms in the hippocampal DG. In recent years, much attention has been paid to brain rhythms observed in local potentials (Buzsáki 2006; Traub and Whittington 2010). Such brain rhythms appear through synchronization between individual neural firings, and they are related to diverse sensory and cognitive functions such as sensory perception, feature integration, selective attention, and memory formation (Wang 2010). At the population level, synchronous small-amplitude fast oscillations [e.g., beta rhythm (15–30 Hz), gamma rhythm (30–100 Hz), and sharp-wave ripple (100–200 Hz)] are shown in local field potential recordings (Fisahn et al. 1998; Csicsvari et al. 1998; Fries et al. 2001; Kim and Lim 2013, 2014, 2015a, b, 2018). On the other hand, at the cellular level, individual cells fire stochastically and sparsely at low rates than the population frequency (Fisahn et al. 1998; Csicsvari et al. 1998; Fries et al. 2001; Kim and Lim 2013, 2014, 2015a, b, 2018). In this way, single-cell firing behavior differs distinctly from population firing behavior. These sparsely synchronized rhythms (SSRs) are in contrast to the fully synchronized large-amplitude slow rhythms where individual cells fire regularly like clock oscillators at the population frequency (Steriade et al. 1993; Destexhe and Sejnowski 2003; Wang 2003).

Here, we first investigate how the adult-born imGCs affect emergence of SSRs of the mGCs and the imGCs in our DG spiking neural network; population and individual firing behaviors in the SSRs are intensively studied. Then, how the SSRs of the mGCs and the imGCs play a role for their encoding functions such as pattern separation and integration is examined. To the best of our knowledge, as a first time, we make quantitative association between SSRs of the mGCs and the imGCs and their pattern separation and integration (facilitating optimal pattern storage in the CA3). They are found to be negatively correlated; the better population and individual behaviors in the SSRs are, the worse their encoding efficacy (through pattern separation and pattern integration) becomes.

This paper is organized as follows. In the main Sect. 2, in our DG spiking neural network (Kim and Lim 2023), we first investigate influence of adult neurogenesis on emergence of SSRs of the mGCs and the imGCs, and then study quantitative association between the SSRs and the efficacy of pattern separation and integration. In the Supplementary Information (SI), brief description on our DG spiking neural network for adult neurogenesis is given. Finally, we provide summary and discussion in Sect. 3.

Influence of adult neurogenesis on emergence of SSRs and quantitative association between SSRs and pattern separation and integration

In this section, we first study influence of adult neurogenesis on emergence of SSRs of the GCs (mGCs and imGCs) in our DG spiking neural network, developed in our prior work (Kim and Lim 2023). Brief description of our DG spiking neural network is given in the SI; for more details, refer to Sec. II in (Kim and Lim 2023). For the imGCs, two competitive properties of high excitability (increasing activation degree) and low excitatory innervation (decreasing activation degree) are considered. Due to low excitatory innervation, the connection probability p_c from the EC cells and the MCs to the imGCs is reduced to 20 x% [x (synaptic connectivity fraction); $0 \le x \le 1$]; in the case of mGCs, $p_c = 20\%$. As x is decreased from 1 to 0, population and individual firing behaviors of the mGCs and the imGCs in their SSRs are investigated by employing the amplitude measure $\mathcal{M}_a^{(X)}$ ($X = m$ and im for the mGCs and the imGCs, respectively) (denoting the population synchronization degree) (Kim and Lim 2021) and the random phase-locking degree $\mathcal{L}_d^{(X)}$ (characterizing regularity of individual single-cell firings) (Kim and Lim 2022a, b), respectively.

In our prior work (Kim and Lim 2023), for $0 \le x \le 1$ the mGCs and the imGCs were found to exhibit pattern separation and pattern integration, respectively. But, their underlying mechanism remains unclear. Here, we examine how the SSRs of the mGCs and the imGCs play a role in the underlying mechanism for pattern separation and integration. Particularly, as a first time, we study quantitative

relationship between $\mathcal{M}_a^{(X)}$ and $\mathcal{L}_d^{(X)}$ of the SSRs and the pattern separation and integration degrees.

Characterization of SSRs in the presence of only the mGCs without the imGCs

In this subsection, we first consider the case of presence of only the mGCs (without the imGCs) to present the methods characterizing the population and individual firing behaviors in the SSRs (Kim and Lim 2022a). Population firing activity of the active mGCs may be well visualized in the raster plot of spikes which is a collection of spike trains of individual active mGCs. Figure 1a1 shows the raster plot of spikes for 120 active mGCs (activation degree D_a of the mGCs is 6%); for convenience, only a part from $t = 300$–1300 ms is shown in the raster plot of spikes. We note that sparsely synchronized stripes (composed of sparse spikes and indicating population sparse synchronization) appear successively.

As a population quantity showing collective behaviors, we employ an IPSR (instantaneous population spike rate) which may be obtained from the raster plot of spikes (Brunel and Wang 2003; Geisler et al. 2005; Brunel and Hakim 2008; Wang 2010; Kim and Lim 2014, 2018). To get the smooth IPSR, we employ the kernel density estimation (kernel smoother) (Shimazaki and Shinomoto 2010). Each spike in the raster plot is convoluted (or blurred) with a kernel function $K_h(t)$ to get a smooth estimate of IPSR $R(t)$:

$$R(t) = \frac{1}{N_a} \sum_{i=1}^{N_a} \sum_{s=1}^{n_i} K_h(t - t_{s,i}), \tag{1}$$

where N_a is the number of the active mGCs, $t_{s,i}$ is the sth spiking time of the ith active mGC, n_i is the total number of spikes for the ith active mGC, and we use a Gaussian kernel function of band width h:

$$K_h(t) = \frac{1}{\sqrt{2\pi}h} e^{-t^2/2h^2}, \quad -\infty < t < \infty, \tag{2}$$

where the band width h of $K_h(t)$ is 20 ms. The IPSR $R(t)$ is also shown in Fig. 1a2. We note that the IPSR $R(t)$ exhibits synchronous oscillation with the population frequency f_p (= 18.2 Hz). The population frequency f_p is given by the reciprocal of the global period T_G (i.e., $f_p = 1/T_G$) which corresponds to the average "intermax" interval (i.e., average interval between neighboring maxima) in the IPSR $R(t)$. Here, we get N_{IMI} (= 545) intermax intervals during the stimulus period T_s ($= 3 \times 10^4$ ms), and get their average value (i.e., global period) T_G (= 54.9 ms). In this way, SSR with f_p (= 18.2 Hz) appears in the (homogeneous) population of active mGCs.

The amplitude of the IPSR $R(t)$ may represent synchronization degree of the SSR. Here, we characterize the synchronization degree of the SSR in terms of the amplitude measure $\mathcal{M}_a$, given by the time-averaged amplitude of $R(t)$ (Kim and Lim 2021):

$$\mathcal{M}_a = \overline{\mathcal{M}_a(j)}; \mathcal{M}_a(j) = \frac{[R_{\max}^{(j)}(t) - R_{\min}^{(j)}(t)]}{2}, \tag{3}$$

where the overline represents time average, $\mathcal{M}_a(j)$ is the amplitude measure in the jth global cycle (corresponding to the jth spiking stripe), and $R_{\max}^{(j)}(t)$ and $R_{\min}^{(j)}(t)$ are the maximum and the minimum of $R(t)$ in the jth global cycle, respectively. As $\mathcal{M}_a$ increases (i.e., the time-averaged amplitude of $R(t)$ is increased), synchronization degree of the SSR becomes higher. Figure 1b shows the plot of the amplitude $\mathcal{M}_a(j)$ versus the spiking stripe index j (corresponding to the global cycle index). We follow the 546 stripes during the stimulus period T_s ($= 3 \times 10^4$ ms), and the amplitude measure $\mathcal{M}_a$ [corresponding to the time-averaged amplitude $\overline{\mathcal{M}_a(j)}$] is thus found to be 3.83.

Next, we consider the individual firing behavior of the active mGCs. For each active mGC, we get the inter-spike-interval (ISI) histogram by collecting the ISIs during the stimulus period T_s ($= 3 \times 10^4$ ms). Each active mGC exhibits intermittent spikings, phase-locked to $R(t)$ at random multiples of its global period T_G (= 54.9 ms). This is in contrast to the case of full synchronization where only

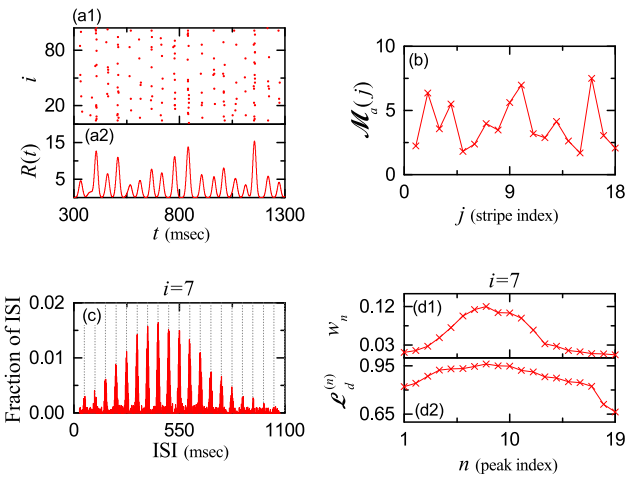

Fig. 1 Characterization of the sparsely synchronized rhythm (SSR) in the presence of only the mGCs without imGCs. **a1** Raster plots of spikes of 120 active mGCs. **a2** Instantaneous population spike rate (IPSR) $R(t)$ of active mGCs. Band width for $R(t)$: $h = 20$ ms. **b** Plot of amplitude measure $\mathcal{M}_a(j)$ of the IPSR $R(t)$ versus j (spiking stripe). **c** Inter-spike-interval (ISI) histogram of the 7th ($i = 7$) active mGC; bin size = 2 ms. Vertical dotted lines in **c** represent the integer multiples of the global period T_G (= 54.9 ms) of $R(t)$. Plots of **d1** normalized weight w_n and **d2** random phase-locking degree $\mathcal{L}_d^{(n)}$ for the nth peak of the ISI histogram for the 7th active mGC versus n (peak index)

one dominant peak appears at the global period T_G; all cells fire regularly at each global cycle without skipping. As a result of random spike skipping, there appear 19 distinct multiple peaks at the integer multiples of T_G in the ISI histogram. These peaks are called as the random-spike-skipping peaks. Then, we get the population-averaged ISI histogram by averaging the individual ISI histograms for all the active mGCs. In this case, the population-averaged ISI ($\langle \text{ISI} \rangle$) of all the active mGCs in the population-averaged ISI histogram is 471.7 ms. Then, the population-averaged mean firing rate (MFR) $\langle f_i \rangle$, given by the reciprocal of $\langle \text{ISI} \rangle$ (i.e., $\langle f_i \rangle = 1/\langle \text{ISI} \rangle$), is 2.12 Hz, which is much less than the population frequency f_p (= 18.2 Hz) of the SSR, in contrast to the case of full synchronization where the population-averaged MFR is the same as the population frequency.

As an example, we consider the case of the 7th ($i = 7$) active mGC. Its ISI histogram is shown in Fig. 1c. In this case, the 8th-order peak is the highest one, and hence spiking may occur most probably after 7-times spike skipping. The nth-order random-spike-skipping peak in the ISI histogram is located as follows:

$$(n - \frac{1}{2})\ T_G < \text{ISI} < (n + \frac{1}{2})\ T_G \qquad \text{for } n \geq 2, \tag{4}$$

$$0 < \text{ISI} < \frac{3}{2}\ T_G \qquad \text{for } n = 1. \tag{5}$$

For each nth-order peak, we obtain the normalized weight w_n, given by:

$$w_n = \frac{N_{\text{ISI}}^{(n)}}{N_{\text{ISI}}^{(tot)}}, \tag{6}$$

where $N_{\text{ISI}}^{(tot)}$ is the total number of ISIs obtained during the stimulus period ($T_s = 3 \times 10^4$ ms) and $N_{\text{ISI}}^{(n)}$ is the number of the ISIs in the nth-order peak. Figure 1d1 shows the plot of w_n versus n (peak index) for all the 19 peaks in the ISI histogram of the 7th ($i = 7$) active mGC. For example, the highest 8th-order peak has $w_8 = 0.12$.

We now consider the sequence of the ISIs, $\{\text{ISI}_j^{(n)},\ j = 1, \ldots, N_{\text{ISI}}^{(n)}\}$, within the nth-order peak, and get the random phase-locking degree $\mathcal{L}_d^{(n)}$ of the nth-order peak (representing how well intermittent spikes make phase-locking to the IPSR $R(t)$ at $t = nT_G$). As in the case of the pacing degree (Kim and Lim 2014), we give a phase ψ to each $\text{ISI}_j^{(n)}$ via linear interpolation:

$$\psi(\Delta\text{ISI}_j^{(n)}) = \frac{\pi}{T_G}\ \Delta\text{ISI}_j^{(n)} \qquad \text{for } n \geq 2, \tag{7}$$

where $\Delta\text{ISI}_j^{(n)} = \text{ISI}_j^{(n)} - n\ T_G$, leading to $-\frac{T_G}{2} < \Delta\text{ISI}_j^{(n)} < \frac{T_G}{2}$. However, for $n = 1$, ψ changes depending on whether the ISI lies in the left or the right part of the 1st-order peak:

$$\psi(\Delta\text{ISI}_j^{(1)}) = \begin{cases} \dfrac{\pi}{2\ T_G}\ \Delta\text{ISI}_j^{(1)} & \text{for } -T_G < \Delta\text{ISI}_j^{(1)} < 0, \\ \dfrac{\pi}{T_G}\ \Delta\text{ISI}_j^{(1)} & \text{for } 0 < \Delta\text{ISI}_j^{(1)} < \dfrac{T_G}{2}, \end{cases} \tag{8}$$

where $\Delta\text{ISI}_j^{(1)} = \text{ISI}_j^{(1)} - T_G$.

Then, the contribution of the $\text{ISI}_j^{(n)}$ to the locking degree $\mathcal{L}_d^{(n)}$ is given by $\cos(\psi_j^{(n)})$; $\psi_j^{(n)} = \psi(\Delta\text{ISI}_j^{(n)})$. An $\text{ISI}_j^{(n)}$ makes the most constructive contribution to $\mathcal{L}_d^{(n)}$ for $\psi_j^{(n)} = 0$, while it makes no contribution to $\mathcal{L}_d^{(n)}$ for $\psi_j^{(n)} = \frac{\pi}{2}$ or $-\frac{\pi}{2}$. By averaging the matching contributions of all the ISIs in the nth-order peak, we get:

$$\mathcal{L}_d^{(n)} = \frac{1}{N_{\text{ISI}}^{(n)}} \sum_{j}^{N_{\text{ISI}}^{(n)}} \cos(\psi_j^{(n)}). \tag{9}$$

Fig. 1d2 shows plot of $\mathcal{L}_d^{(n)}$ versus n (peak index) for the 19 random-spike-skipping peaks in the ISI histogram of the 7th active mGC. For example, the highest 8th-order ($n = 8$) peak has the maximum value of $\mathcal{L}_d^{(n)}$ (= 0.961). Through weighted average of the random phase-locking degrees $\mathcal{L}_d^{(n)}$ of all the peaks, we obtain the (overall) random phase-locking degree $\mathcal{L}_d$

$$\mathcal{L}_d = \sum_{n=1}^{N_p} w_n \cdot \mathcal{L}_d^{(n)} = \frac{1}{N_{\text{ISI}}^{(\text{tot})}} \sum_{n=1}^{N_p} \sum_{j=1}^{N_{\text{ISI}}^{(\text{tot})}} \cos(\psi_j^{(n)}), \tag{10}$$

where N_p is the number of peaks in the ISI histogram. We note that, $\mathcal{L}_d$ corresponds to the average of contributions of all the ISIs in the ISI histogram. In the case of the 7th active mGC, the random phase-locking degree $\mathcal{L}_d$, characterizing the sharpness of all the peaks, is 0.92. Hence, the mGCs make intermittent spikes which are well phase-locked to $R(t)$ at random multiples of its global period T_G.

We repeat the above process in the ISI histogram of each ith ($i = 1, \ldots, 120$) active mGC and get its random phase-locking degree $\mathcal{L}_d(i)$. The range of $\{\mathcal{L}_d(i)\}$ is [0.77, 0.98]. Then, the random phase-locking degree $\mathcal{L}_d$ of all the active mGCs ia given by the average value (= 0.92) of the distribution $\{\mathcal{L}_d(i)\}$.

Influence of the adult-born imGCs on emergence of SSRs and their population and individual firing behaviors

In this subsection, we consider a heterogeneous population, composed of mGCs and imGCs; fraction of the imGCs in the whole population is 10%. As shown in Fig. 2 in Kim

and Lim (2023), as a result of increased leakage reversal potential V_L, the imGC has lower firing threshold than the mGC (i.e., high excitability), which results in high activation of the imGC (Sahay et al. 2011a, b; Spalding et al. 2013; Boldrini et al. 2018; Gage 2019; Wang et al. 2020). We also note that, the imGC has low excitatory innervation from the EC cells and the hilar MCs, counteracting its high excitability (Aimone et al. 2011). In the case of the mGCs, the connection probability p_c from the EC cells and the MCs to the mGCs is 20%, while in the case of the imGCs, p_c is decreased to 20 x % [x : synaptic connectivity fraction; $0 \le x \le 1$]. Due to low excitatory drive from the EC cells and the MCs, the activation degree of the imGCs becomes reduced. With decreasing x from 1 to 0, we investigate the influence of high excitability and low excitatory innervation for the imGCs on the population and individual firing behaviors of the mGCs and the imGCs in their SSRs. We also note that, for $0 \le x \le 1$ the mGCs and the imGCs were found to exhibit pattern separation and pattern integration, respectively (Kim and Lim 2023). Hence, we also study quantitative relationship between SSRs and pattern separation and integration.

Here, as in the case of Fig. 1, we consider a long-term stimulus stage (300–30,300 ms) (i.e., the stimulus period $T_s = 30,000$ ms), because long-term stimulus is necessary for analysis of dynamical behaviors. Population firing activity of the active mGCs and imGCs may be well visualized in the raster plot of spikes which is a collection of spike trains of individual active GCs. Figure 2a1–a4 show the raster plots of spikes for the active mGCs (red) and imGCs (blue) for $x = 1.0$, 0.7, 0.4, and 0.2, respectively. For convenience, only a part from $t = 300$–1300 ms is shown in each raster plot of spikes. We note that sparsely synchronized stripes (composed of sparse spikes and indicating population sparse synchronization) appear successively; overall, the pacing degree between spikes in the spiking stripes is low. In the case of mGCs, with decreasing x from 1 their spiking stripes become clearer, while in the case of imGCs their stripes become more smeared.

The IPSR (showing population firing behavior) may be obtained from the raster plot of spikes [see Eq. (1)]. The IPSRs $R^{(X)}(t)$ of the mGCs ($X = m$: red) and the imGCs ($X = im$: blue) are shown in Fig. 2a1–a4 for $x = 1.0$, 0.7, 0.4 and 0.2, respectively. We note that $R^{(X)}(t)$ exhibit synchronous oscillations. But, the average amplitude of $R^{(X)}(t)$ in each case of mGCs and imGCs is smaller than that in the case of homogeneous population of only mGCs in Fig. 1a2, and variations in the amplitudes are also large.

For $x = 1$, imGCs fire spikings much more actively than mGCs because the imGCs have high excitability. On the other hand, firing activity of mGCs becomes much decreased due to strongly increased feedback inhibition from the BCs and the HIPP cells. Hence, in the case of $x = 1$ the amplitude of $R^{(im)}(t)$ (blue) of the imGCs is larger than that of $R^{(m)}(t)$ (red) of the mGCs. However, as x is decreased from 1, firing activity of the imGCs becomes

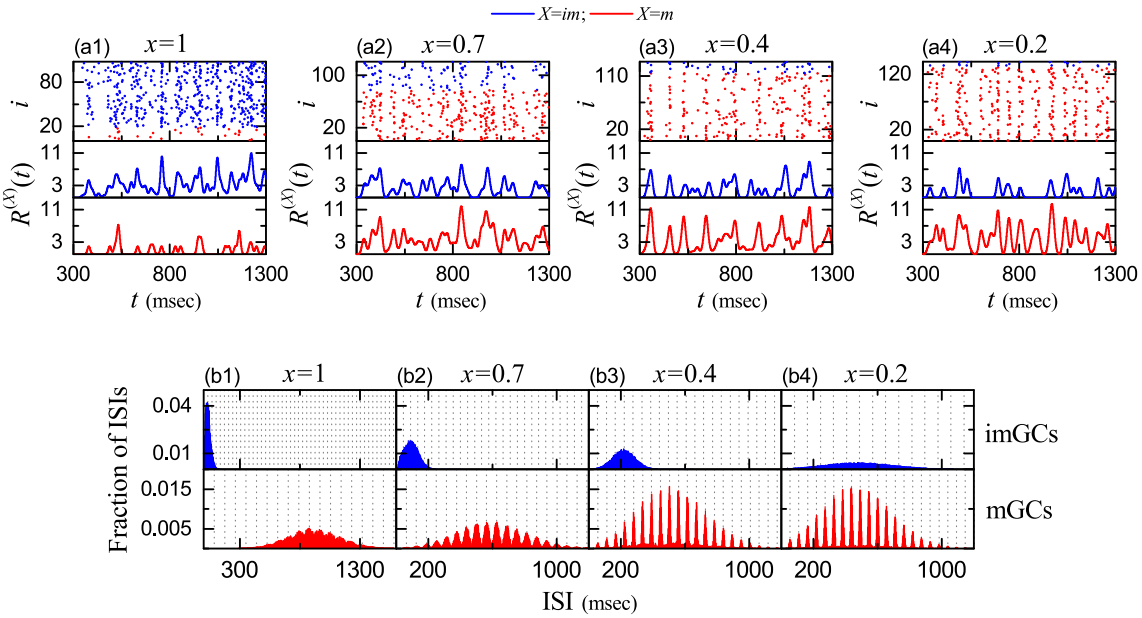

Fig. 2 SSRs and multi-peaked ISI histograms in each case of the imGCs and the mGCs. **a1–a4** Raster plots of spikes and IPSRs $R^{(X)}(t)$ for the active imGCs ($X = im$) and the mGCs ($X = m$) when x (synaptic connectivity fraction) is 1.0, 0.7, 0.4, and 0.2, respectively. **b1–b4** Population-averaged ISI histograms for the active imGC and mGC when $x = 1.0$, 0.7, 0.4, and 0.2, respectively; bin size = 2 ms. Vertical dotted lines in **b1–b4** represent the integer multiples of the global period $T_G^{(X)}$ of $R^{(X)}(t)$. In **a1–a4** and **b1–b4**, imGCs and imGCs are denoted in blue and red color, respectively

rapidly reduced (i.e., the influence of imGCs decreases rapidly) because of low excitatory innervation from the EC cells and the MCs. On the other hand, firing activity of mGCs becomes enhanced due to decrease in the feedback inhibition into the mGCs from the BCs and the HIPP cells. Thus, with decreasing x from 1, the amplitude of $R^{(m)}(t)$ of the mGCs makes an increase because the pacing degree between spikes in each spiking stripe in the rater plot of spikes becomes better (i.e., the spiking stripes in the raster plot of spikes become clearer). In contrast, in the case of imGCs, the amplitude of $R^{(im)}(t)$ decreases because the pacing degree of spikes in the raster plot becomes worse (i.e., the spiking stripes in the raster plot of spikes become smeared). Thus, for example, for $x = 0.2$ the amplitude of $R^{(m)}(t)$ becomes much larger than that of $R^{(im)}(t)$.

In addition to the (above) population firing activity, we also study the individual spiking activity of the active GCs. In each case of the mGCs ($X = m$) and the imGCs ($X = im$), we get the ISI histogram for each active GC by collecting the ISIs during the stimulus period T_s ($= 3 \times 10^4$ ms), and then obtain the population-averaged ISI histogram by averaging the individual ISI histograms for all the active GCs. Figure 2b1–b4 show the population-averaged ISI histograms for $x = 1$, 0.7, 0.4, and 0.2, respectively.

We first consider the case of $x = 1$ in Fig. 2b1. For the mGCs (red), each active mGC exhibits intermittent spikings, phase-locked to $R^{(m)}(t)$ at random multiples of its global period $T_G^{(m)}$ (= 87.8 ms) [corresponding to the average "intermax" interval between neighboring maxima in $R^{(m)}(t)$]; vertical dotted lines represent integer multiples of the global period $T_G^{(m)}$ of $R^{(m)}(t)$. As a result of random spike skipping, there appear 12 multiple peaks in the ISI histogram. The middle 10th-order peak is the highest one, and hence spiking may occur most probably after 9-times spike skipping. This is in contrast to the case of full synchronization where only one dominant peak appears at the global period T_G of the IPSR $R(t)$; all cells fire regularly at each global cycle without skipping. Next, we consider the case of imGCs (blue). Its ISI histogram has a single peak near the global period $T_G^{(im)}$ ($= 34.3$ ms) of the IPSR $R^{(im)}(t)$ and its distribution is broadly extended to $\sim 3\ T_G^{(im)}$. The imGCs exhibit spikes mainly at $T_G^{(im)}$ (i.e., they fire mainly in each stripe), but they also show intermittent spikings at 2 $T_G^{(im)}$ or 3 $T_G^{(im)}$ (i.e., spike skippings also occur).

As x is decreased from 1 (i.e., considering low excitatory innervation for the imGCs), the influence of the imGCs becomes weaker. In this case, the imGCs show more irregular spiking behaviors. Hence, their single-peaked ISI histograms become broader, as shown in Fig. 2b2–b4 for $x = 0.7$, 0.4, and 0.2, respectively. The order n of peak also increases with decreasing x ($n = 2$, 4, and 6 for $x = 0.7$, 0.4, and 0.2, respectively). Hence, more spike skippings occur. On the other hand, with decreasing x from 1, the mGCs exhibit more regular spiking behaviors. Hence, their ISI histograms become clearer because multiple peaks become sharper and their heights become increased [see Fig. 2b2–b4].

From now on, in Fig. 3, we quantitatively characterize population and individual firing behaviors in the SSRs of the mGCs ($X = m$) and the imGCs ($X = im$). We first consider the population firing behaviors which are well shown in $R^{(X)}(t)$. Figure 3a shows the plots of the population frequency $f_p^{(X)}$ [i.e., the average oscillating frequency of $R^{(X)}(t)$, corresponding to the reciprocal of the global period $T_G^{(X)}$ of the SSRs for $X = m$ (red crosses) and im (blue open circles)]. For $x = 1$, $f_p^{(im)}$ (= 29.2 Hz) for the imGCs is faster than $f_p^{(m)}$ (= 11.4 Hz) for the mGCs, as can be well seen in Fig. 2a1, mainly because for $x = 1$ firing of the imGCs is much more active than that of the mGCs (resulting from high excitability of the imGCs).

However, as x is decreased from 1 to 0, $f_p^{(im)}$ decreases to 0 rapidly due to rapid decrease in firing activity of the imGCs (resulting from their low excitatory innervation). On the other hand, $f_p^{(m)}$ increases to 18.6 Hz because of increase in firing activity of the mGCs (resulting from

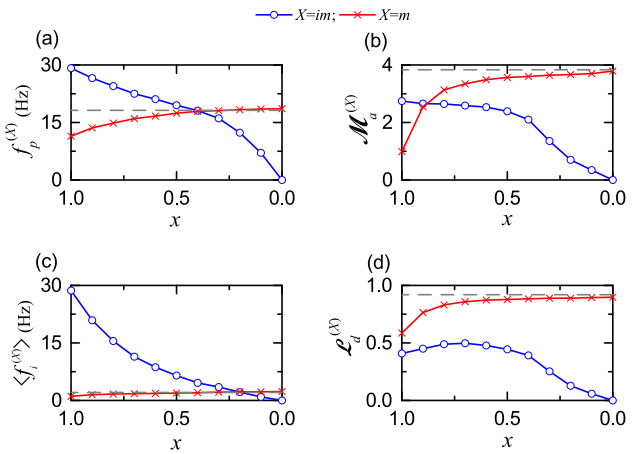

Fig. 3 Population and individual firing behaviors in the SSRs of the imGCs ($X = im$) and the mGCs ($X = m$). **a** Plots of the population frequencies $f_p^{(X)}$ versus x (synaptic connectivity fraction). **b** Plots of the amplitude measures $\mathcal{M}_a^{(X)}$ versus x. **c** Plots of the population-averaged mean firing rates $\langle f_i^{(X)} \rangle$ versus x. **d** Plots of the random-phase-locking degrees $\mathcal{L}_d^{(X)}$ versus x. Horizontal dashed lines in **a**–**d** represent f_p (= 18.2 Hz), M_a (= 3.83), $\langle f_i \rangle$ (= 2.12 Hz), and $\mathcal{L}_d$ (= 0.92) in the presence of only mGCs (without imGCs), respectively. The mGCs and imGCs are denoted by red crosses and blue open circles, respectively

decrease in the feedback inhibition into the mGCs). We note that, $f_p^{(im)}$ and $f_p^{(m)}$ cross at $x^* \sim 0.4$; for $x > x^*$ $f_p^{(im)} > f_p^{(m)}$, while for $x < x^*$ $f_p^{(m)} > f_p^{(im)}$. We also note that, for $x = 0$ $f_p^{(m)}$ (= 18.6 Hz) is a little larger than the dashed horizontal line ($f_p = 18.2$ Hz) in the homogeneous population of only the mGCs (without imGCs), which may be understood as follows. In the limiting case of $x = 0$, the imGCs become completely inactive. Hence, the feedback inhibition (from the BCs and the HIPP cells) to the mGCs becomes reduced in comparison to the homogeneous case consisting of only mGCs, which results in increased firing activity of the mGCs in the heterogeneous population of mGCs and imGCs.

The amplitude of the IPSR $R^{(X)}(t)$ may represent synchronization degree of the SSR. Thus, we characterize the synchronization degree of the SSRs of the mGCs ($X = m$) and the imGCs ($X = im$) in terms of the amplitude measure $\mathcal{M}_a^{(X)}$ of Eq. (3), given by the time-averaged amplitude of $R^{(X)}(t)$. Fig. 3b shows the plots of $\mathcal{M}_a^{(X)}$ versus x for the mGCs (red crosses) and the imGCs (blue open circles). For $x = 1$ (i.e., high excitability of the imGCs), $\mathcal{M}_a^{(im)}$ (= 2.75) for the imGCs is larger than $\mathcal{M}_a^{(m)}$ (= 0.99) for the mGCs, as can be seen well in Fig. 2a1, because the imGCs fire more actively and coherently than the mGCs.

As x is decreased from 1 to 0 (i.e., low excitatory innervation to the imGCs) the influence of imGCs becomes decreased rapidly, which results in more active and coherent firing activity of the mGCs (due to decreased feedback to the mGCs from the BCs and the HIPP cells). Consequently, $\mathcal{M}_a^{(m)}$ increases to 3.79, while $\mathcal{M}_a^{(im)}$ decreases to 0. We note that the limit value (= 3.79) of $\mathcal{M}_a^{(m)}$ is a little smaller than $\mathcal{M}_a$ (= 3.83) in the homogeneous population of only the mGCs (without imGCs) [represented by the dashed horizontal line in Fig. 3b]. Hence, for all x, $\mathcal{M}_a^{(X)}$ of the mGCs and the imGCs is less than that (= 3.83) in the homogeneous case consisting of only mGCs. Consequently, in the whole range of x, due to heterogeneity caused by the imGCs, population firing behaviors (characterized in terms of $\mathcal{M}_a^{(X)}$) of mGCs and imGCs in their SSRs become deteriorated, in comparison to that in the presence of only mGCs (without imGCs).

Next, we consider the individual firing behaviors of the active mGCs and imGCs which are well shown in their ISI histograms. Figure 3c shows the plots of the population-averaged MFRs $\langle f_i^{(X)} \rangle$ of the individual mGCs ($X = m$: red crosses) and imGCs ($X = im$: blue open circles); $\langle f_i^{(X)} \rangle$ corresponds to the reciprocal of the population-averaged ISI ($\langle \text{ISI} \rangle^{(X)}$) (i.e., $\langle f_i^{(X)} \rangle = 1/\langle \text{ISI} \rangle^{(X)}$) in the population-averaged ISI histogram of the X-population.

For $x = 1$, $\langle f_i^{(im)} \rangle$ (= 28.7 Hz) for the imGCs is much faster than $\langle f_i^{(m)} \rangle$ (= 1.12 Hz) for the mGCs, as can be well seen in Fig. 2b1. In this case, due to their high excitability, the imGCs exhibit active firing activity, while the mGCs show very intermittent spikings due to strong feedback inhibition (from the BCs and the HIPP cells). Thus, in the case of mGCs the population-averaged MFR $\langle f_i^{(m)} \rangle$ is much less than the population frequency $f_p^{(m)}$ (= 11.4 Hz) for the SSR, due to random spike skipping, which is in contrast to the case of full synchronization where the population-averaged MFR is the same as the population frequency. On the other hand, in the case of imGCs, their population-averaged MFR $\langle f_i^{(im)} \rangle$ is close to the population frequency $f_p^{(im)}$ (= 29.2 Hz) for the SSR, and hence the active imGCs show nearly fully synchronized rhythm (i.e., most of all active imGCs fire in each spiking stripe) in the case of $x = 1$.

However, as x is decreased from 1 to 0, firing activity of imGCs is decreased rapidly due to low excitatory innervation. Consequently, $\langle f_i^{(im)} \rangle$ decreases so rapidly from 28.7 Hz to 0. Thus, for $x < 1$, active imGCs distinctly exhibit random spike skipping, leading to SSR with $f_p^{(im)} > \langle f_i^{(im)} \rangle$. On the other hand, with decreasing x from 1, $\langle f_i^{(m)} \rangle$ of the mGCs increases slowly from 1.12 to 2.30 Hz, because of decrease in feedback inhibition to the mGCs. When passing a threshold ($x \sim 0.3$), $\langle f_i^{(m)} \rangle$ crosses the horizontal dashed line (= 2.12 Hz), representing the population-averaged MFR in the presence of only the mGCs (without the imGCs). It also crosses the decreasing curve of $\langle f_i^{(im)} \rangle$ for $x \sim 0.2$, and then converges to the limit value (= 2.30 Hz).

Next, we characterize the degree of random spike skipping seen in the ISI histograms in the case of $X = m$ and im in terms of the random phase-locking degree $\mathcal{L}_d^{(X)}$ of Eq. (10) (denoting how well intermittent spikes make phase-locking to the IPSR $R^{(X)}(t)$ at random multiples of its global period $T_G^{(X)}$). The sharper the random-spike-skipping peaks in the ISI histogram are, the larger $\mathcal{L}_d^{(X)}$ becomes.

Figure 3d shows the plots of $\mathcal{L}_d^{(X)}$ versus x for the mGCs ($X = m$: red crosses) and the imGCs ($X = im$: blue open circles). In the case of mGCs, multi-peaked ISI histograms appear due to random spike skippings. As x is decreased from 1, their ISI histograms become clearer because multiple peaks become sharper and their heights become increased. Thus, with decreasing x from 1 to 0, $\mathcal{L}_d^{(m)}$ is found to increase from 0.587 to 0.898. On the other hand, the ISI histograms for the imGCs have single peaks. As x is

decreased from 1, their single-peaked ISI histograms become broader, which leads to more random spike skippings. But, at first, in the nth global cycle where the single peak exists [e.g., $n = 1$ (2) for $x = 1.0$ (0.7)], the random phase locking degree $\mathcal{L}_d^{(im)}(n)$ increases a little until x is decreased to $x^*(\sim 0.7)$. Thus, as x is decreased from 1 to x^*, the overall $\mathcal{L}_d^{(im)}$ increases a little from 0.408 to 0.497. Then, for $x < x^*$, $\mathcal{L}_d^{(im)}$ decreases rapidly to 0, in contrast to the case of mGCs.

We also note that, in the limiting case of $x = 0$, $\mathcal{L}_d^{(m)}$ (= 0.898) is smaller than $\mathcal{L}_d$ (= 0.92) in the homogeneous population of only the mGCs (without imGCs) [represented by the dashed curve in Fig. 3d]. Hence, for all x, $\mathcal{L}_d^{(X)}$ of the mGCs and the imGCs is smaller than that (= 0.92) in the homogeneous case composed of only mGCs. As a result, in the whole range of x, because of heterogeneity caused by the imGCs, individual firing behaviors (characterized in terms of $\mathcal{L}_d^{(X)}$) of mGCs and imGCs in their SSRs become deteriorated, in comparison with the homogeneous case consisting of only mGCs (without imGCs).

Quantitative relationship between SSRs and pattern separation and integration

In this subsection, we examine how the SSRs of the mGCs and the imGCs are associated with their encoding functions such as pattern separation and integration. In our prior work (Kim and Lim 2023), by varying the synaptic connectivity fraction x, we studied pattern separation (transforming similar input patterns into less similar output patterns) of the mGCs ($X = m$) in terms of the pattern separation degree $\mathcal{S}_d^{(X)}$ [see Fig. 4e in Kim and Lim (2023)]. The pattern separation degree $\mathcal{S}_d^{(X)}$ is given by the ratio of $D_p^{(out)}$ (pattern distance for the output pattern pair) to $D_p^{(in)}$ (pattern distance for the input pattern pair) [see Eq. (17) in (Kim and Lim 2023)]. For $\mathcal{S}_d^{(X)} > 1$ pattern separation occurs, because the output pattern pair of the mGCs is more dissimilar than the input pattern pair of the EC cells. On the other hand, for $\mathcal{S}_d^{(X)} < 1$ no pattern separation occurs; instead, pattern convergence takes place. For the mGCs, with decreasing x from 1, $\mathcal{S}_d^{(m)}$ was found to decrease from a high value (= 13.142) for $x = 1$ to a limit value (= 1.495) for $x = 0$, as shown in Fig. 4e in Kim and Lim (2023). Thus, in the whole range of $0 \le x \le 1$, the mGCs perform good pattern separation with $\mathcal{S}_d^{(m)} > 1$.

In contrast to the mGCs, the imGCs exhibit pattern integration (making association between dissimilar patterns), characterized in terms of the integration degree $\mathcal{I}_d$. $\mathcal{I}_d$ is given by the ratio of the average pattern correlation degree for the output pattern pair of the imGCs to the average pattern correlation degree for the input pattern pair of the EC cells [see Eq. (18) in (Kim and Lim 2023)]. For $x = 1$ the pattern integration degree $\mathcal{I}_d$ of the imGCs is high (1.9559). With decreasing x from 1 to 0, $\mathcal{I}_d$ was found to increase from 1.9559 to 2.2502, as shown in Fig. 4f in Kim and Lim (2023). Thus, in the whole range of $0 \le x \le 1$, the imGCs are good pattern integrators with $\mathcal{I}_d > 1$.

We investigate quantitative relationship between SSRs of the mGCs and the imGCs and their pattern separation and integration. Figure 4a1 and a2 show the plots of the pattern separation degree $\mathcal{S}_d^{(X)}$ versus $\mathcal{M}_a^{(X)}$ and $\mathcal{S}_d^{(X)}$ versus $\mathcal{L}_d^{(X)}$ for $X = m$ (mGCs), respectively. $\mathcal{S}_d^{(m)}$ for the mGCs is found to be negatively correlated with $\mathcal{M}_a^{(X)}$ and $\mathcal{L}_d^{(X)}$ of their SSR with the Pearson's correlation coefficients $r = -0.9994$ and -0.9998, respectively (Pearson 1895). Thus, in the population of the mGCs, the better population and individual firing behaviors in their SSR are, the worse their pattern separation becomes.

In the case of $X = im$ (imGCs), plots of the pattern integration degree $\mathcal{I}_d$ versus $\mathcal{M}_a^{(im)}$ and $\mathcal{I}_d$ versus $\mathcal{L}_d^{(im)}$ are shown in Figs. 4b1-b2, respectively. As in the case of mGCs, $\mathcal{I}_d$ for the imGCs is also negatively correlated with $\mathcal{M}_a^{(im)}$ with the Pearson's correlation coefficients $r = -0.8483$. Next, we consider quantitative relationship between $\mathcal{I}_d$ and $\mathcal{L}_d^{(im)}$. As shown in Fig. 3d, for $1.0 \ge x \ge 0.7$, $\mathcal{L}_d^{(im)}$ makes a small increase, and then for $x \le 0.7$ it rapidly decreases to 0. Thus, $\mathcal{I}_d$ is also negatively correlated with $\mathcal{L}_d^{(im)}$ in the range of $0.7 \ge x \ge 0$ with the

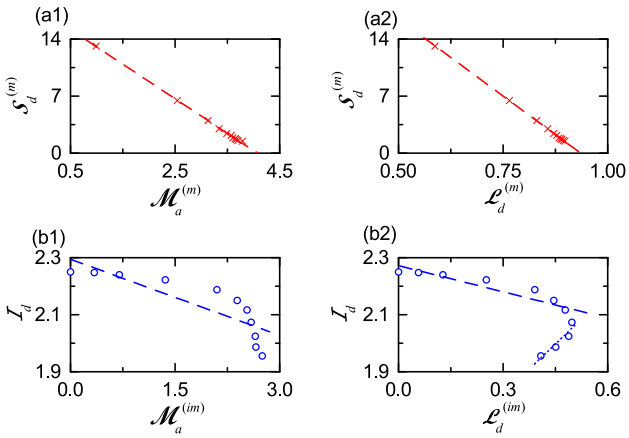

Fig. 4 Quantitative relationship between SSRs and pattern separation and integration in each case of mGCs and imGCs. In the case of mGCs, plots of **a1** the pattern separation degree $\mathcal{S}_d^{(m)}$ versus $\mathcal{M}_a^{(m)}$ and **a2** $\mathcal{S}_d^{(m)}$ versus $\mathcal{L}_d^{(m)}$. In the case of imGCs, plots of **b1** the pattern integration degree $\mathcal{I}_d$ versus $\mathcal{M}_a^{(im)}$ and b2 $\mathcal{I}_d$ versus $\mathcal{L}_d^{(im)}$. Fitted dashed lines are given in **a1**–**b1**. In **b2**, fitted dashed and dotted lines are obtained from 8 data points for $0.7 \le x \le 0$ and 4 data points for $1 \le x \le 0.7$, respectively

Pearson's correlation coefficients $r = -0.9159$, as in the case of $\mathcal{M}_a^{(im)}$, while in the initial small range of $1.0 \geq x \geq 0.7$, $\mathcal{I}_d$ is positively correlated with $\mathcal{L}_d^{(im)}$ with the Pearson's correlation coefficients $r = 0.9365$. Thus, in the population of the imGCs, for $0.7 \geq x \geq 0$ the better population and individual firing behaviors in their SSR are, the worse their integration becomes.

Summary and discussion

We first studied influence of the adult-born imGCs on emergence of SSRs of the main-encoding GCs (mGCs and imGCs) in our DG spiking neural network. Then, we examined how the SSRs of the mGCs and the imGCs play a role in pattern separation and integration (facilitating optimal pattern storage in the CA3). Particularly, as a first time, quantitative association between the SSRs and the pattern separation and integration was made.

The imGCs show two marked properties; (1) high excitability (increasing activation degree) and (2) low excitatory innervation (decreasing activation degree). Thus, the influence of low excitatory innervation counteracts the influence of high excitability. The connection probability p_c from the EC cells and the MCs to the imGCs is 20 x % [x (synaptic connectivity fraction); $0 \leq x \leq 1$], in contrast to the case of mGCs with $p_c = 20\%$. As x is decreased from 1 to 0, SSRs of the mGCs and the imGCs were found to emerge, and population and individual firing behaviors in the SSRs were characterized in terms of the amplitude measure $\mathcal{M}_a^{(X)}$ ($X = m$ and im) and the random phase-locking degree $\mathcal{L}_d^{(X)}$, respectively.

As shown in Fig. 3, as x is decreased from 1, the amplitude measure $\mathcal{M}_a^{(m)}$ and the random phase-locking degree $\mathcal{L}_d^{(m)}$ were found to increase in the case of mGCs. With decreasing x from 1, influence of the imGCs became weaker, which resulted in increase in $\mathcal{M}_a^{(m)}$ and $\mathcal{L}_d^{(m)}$ for the mGCs. In contrast, as x decreases from 1, $\mathcal{M}_a^{(im)}$ of the imGCs was found to monotonically decrease, and their $\mathcal{L}_d^{(im)}$ was found to first slowly a little increase and then rapidly decrease to zero (i.e., for $x < 0.7$, monotonic decrease to zero occurs). In this way, the changing tendency for the imGCs was in contrast to that of the mGCs. We also note that in the heterogeneous population (consisting of the mGCs and the imGCs), $\mathcal{M}_a^{(X)}$ and $\mathcal{L}_d^{(X)}$ ($X = m$ and im) were less than those in the homogeneous population of only mGCs without imGCs. Due to heterogeneity caused by the imGCs, the population and individual firing behaviors of the GCs in the SSRs became deteriorated, in comparison with those in the presence of only mGCs (without imGCs).

In our prior work (Kim and Lim 2023), in the whole range of x (i.e., for $1 \geq x \geq 0$), the mGCs and the imGCs were found to exhibit pattern separation and pattern integration, respectively. As x is decreased from 1, the pattern separation degree $\mathcal{S}_d^{(m)}$ of the mGCs was found to decrease, as shown in Fig. 4e in Kim and Lim (2023), because their activation degree increased. In contrast to the mGCs, the imGCs was found to show pattern integration, and its degree $\mathcal{I}_d$ was found to increase as x is decreased from 1, due to increase in correlation between the imGCs [see Fig. 4f in Kim and Lim (2023)]. But, the underlying dynamical mechanism for pattern separation and integration remains unclear. We examined how the SSRs of the mGCs and the imGCs are associated with their encoding functions such as pattern separation and integration. Quantitative relationship between SSRs and pattern separation and integration was shown in Fig. 4. $\mathcal{S}_d^{(m)}$ for the mGCs was found to be negatively correlated with $\mathcal{M}_a^{(m)}$ and $\mathcal{L}_d^{(m)}$ of their SSRs. Thus, in the population of the mGCs, the better population and individual firing behaviors in their SSRs are, the worse their pattern separation efficacy becomes. Also, in the case of imGCs, for $0.7 \geq x \geq 0$, $\mathcal{I}_d$ was found to be negatively correlated to $\mathcal{M}_a^{(im)}$ and $\mathcal{L}_d^{(im)}$ of their SSRs. Hence, in the population of imGCs, for $0.7 \geq x \geq 0$, the better population and individual firing behaviors in their SSRs are, the worse their pattern integration efficacy becomes.

Finally, we summarize our main results. The DG is the gateway to the hippocampus. Encoding cortical inputs in the DG facilitates pattern storage in the CA3. Distinctly, young imGCs appear in the DG through adult neurogenesis. Our main concern is to study the influence of imGCs on the encoding functions in the DG. As is well known, the mGCs and the imGCs in the DG exhibit pattern separation and pattern integration (Kim and Lim 2023). The pattern separation (integration) efficacy of the mGCs (imGCs) becomes better for similar (dissimilar) input patterns. Thus, in a heterogeneous population of mGCs (pattern separators) and imGCs (pattern integrators), the memory storage capacity could be optimized through cooperative interplay via pattern separation and pattern integration.

We note that, during such pattern separation and integration, SSRs were found to emerge in the populations of the mGCs and the imGCs. We first studied influence of adult-born imGCs on population and individual firing behaviors in the SSRs of mGCs and imGCs. Then, we investigated quantitative relationship between the SSRs of the mGCs and the imGCs and their encoding functions (i.e., pattern separation and pattern integration). They were

found to be negatively correlated; the better population and individual behaviors in the SSRs are, the worse their encoding efficacy (via pattern separation and pattern integration) becomes. To the best of our knowledge, as a first time, we made quantitative association between SSRs of the mGCs and the imGCs and their pattern separation and integration (facilitating optimal pattern storage in the CA3). However, this kind of negative correlations do not imply causal relationship. Hence, in future work, it would be interesting to intensively investigate their dynamical causation.

Supplementary Information The online version contains supplementary material available at https://doi.org/10.1007/s11571-024-10089-x.

Acknowledgements This research was supported by the Basic Science Research Program through the National Research Foundation of Korea (NRF) funded by the Ministry of Education (Grant No. 20162007688).

Declaration

Conflict of interest The authors declare that they have no conflict of interest.

References

Aimone JB, Wiles J, Gage FH (2009) Computational influence of adult neurogenesis on memory encoding. Neuron 61:187–202

Aimone JB, Deng W, Gage FH (2011) Resolving new memories: a critical look at the dentate gyrus, adult neurogenesis, and pattern separation. Neuron 70:589–596

Altman J (1962) Are new neurons formed in the brains of adult mammals? Science 135:1127–1128

Altman J (1963) Autoradiographic investigation of cell proliferation in the brains of rats and cats. Anat Rec 145:573–591

Altman J, Das GD (1965) Autoradiographic and histological evidence of postnatal hippocampal neurogenesis in rats. J Comp Neurol 124:319–335

Bakker A, Kirwan CB, Miller M, Stark CEL (2008) Pattern separation in the human hippocampal CA3 and dentate gyrus. Science 319:1640–1642

Bayer SA (2016) Joseph Altman (1925–2016): a life in neurodevelopment. J Comp Neurol 524:2933–2944

Beck H, Goussakov IV, Lie A, Helmstaedter C, Elger CE (2000) Synaptic plasticity in the human dentate gyrus. J Neurosci 20:7080–7086

Boldrini M, Fulmore CA, Tartt AN, Simeon LR, Pavlova I, Poposka V, Rosoklija GB, Stankov A, Arango V, Dwork AJ, Hen R, Mann JJ (2018) Human hippocampal neurogenesis persists throughout aging. Cell Stem Cell 22:589-599.e5

Brunel N, Hakim V (2008) Sparsely synchronized neuronal oscillations. Chaos 18:015113

Brunel N, Wang XJ (2003) What determines the frequency of fast network oscillations with irregular neural discharges? I. Synaptic dynamics and excitation-inhibition balance. J Neurophysiol 90:415–430

Buzsáki G (2006) Rhythms of the brain. Oxford University Press, New York

Chavlis S, Petrantonakis PC, Poirazi P (2017) Dendrites of dentate gyrus granule cells contribute to pattern separation by controlling sparsity. Hippocampus 27:89–110

Christian KM, Ming GI, Song H (2020) Adult neurogenesis and the dentate gyrus: predicting function from form. Behav Brain Res 379:112346

Csicsvari J, Hirase H, Czurko A, Buzsáki G (1998) Reliability and state dependence of pyramidal cell-interneuron synapses in the hippocampus: an ensemble approach in the behaving rat. Neuron 21:179–189

Destexhe A, Sejnowski TJ (2003) Interactions between membrane conductances underlying thalamocortical slow-wave oscillations. Physiol Rev 83:1401–1453

Dieni CV, Panichi R, Aimone JB, Kuo CT, Wadiche JI, Overstreet-Wadiche L (2016) Low excitatory innervation balances high intrinsic excitability of immature dentate neurons. Nat Commun 7:11313

Fisahn A, Pike FG, Buhl EH, Paulsen O (1998) Cholinergic induction of network oscillations at 40 Hz in the hippocampus in vitro. Nature 394:186–189

Fries P, Reynolds JH, Rorie AE, Desimone R (2001) Modulation of oscillatory neuronal synchronization by selective visual attention. Science 291:1560–1563

Gage FH (2019) Adult neurogenesis in mammals. Science 364:827–828

Geisler C, Brunel N, Wang XJ (2005) Contributions of intrinsic membrane dynamics to fast network oscillations with irregular neuronal discharges. J Neurophysiol 94:4344–4361

Gluck MA, Myers CE (2001) Gateway to memory: an introduction to neural network modeling of the hippocampus in learning and memory. MIT Press, Cambridge

Kassab R, Alexandre F (2018) Pattern separation in the hippocampus: distinct circuits under different conditions. Brain Struct Funct 223:2785–2808

Kim SY, Lim W (2013) Sparsely-synchronized brain rhythm in a small-world neural network. J Korean Phys Soc 63:104–113

Kim SY, Lim W (2014) Realistic thermodynamic and statistical-mechanical measures for neural synchronization. J Neurosci Methods 226:161–170

Kim SY, Lim W (2015a) Effect of small-world connectivity on fast sparsely synchronized cortical rhythms. Physica A 421:109–123

Kim SY, Lim W (2015b) Fast sparsely synchronized brain rhythms in a scale-free neural network. Phys Rev E 92:022717

Kim SY, Lim W (2018) Effect of inhibitory spike-timing-dependent plasticity on fast sparsely synchronized rhythms in a small-world neuronal network. Neural Netw 106:50–66

Kim SY, Lim W (2021) Equalization effect in interpopulation spike-timing-dependent plasticity in two inhibitory and excitatory populations. In: Lintas A, Enrico P, Pan X, Wang R, Villa A (eds) Advances in cognitive neurodynamics (VII). Springer, Singapore, Ch, p 8

Kim SY, Lim W (2022a) Population and individual firing behaviors in sparsely synchronized rhythms in the hippocampal dentata gyrus. Cogn Neurodyn 16:643–665

Kim SY, Lim W (2022b) Disynaptic effect of hilar cells on pattern separation in a spiking neural network of hippocampal dentate gyrus. Cogn Neurodyn 16:1427–1447

Kim SY, Lim W (2023) Effect of adult-born immature granule cells on pattern separation in the hippocampal dentate gyrus. Cogn Neurodyn. https://doi.org/10.1007/s11571-023-09985-5

Knierim JJ, Neunuebel JP (2016) Tracking the flow of hippocampal computation: pattern separation, pattern completion, and attractor dynamics. Neurobiol Learn Mem 129:38–49

Leutgeb JK, Leutgeb S, Moser MB, Moser EI (2007) Pattern separation in the dentate gyrus and CA3 of the hippocampus. Science 315:961–966

Marr D (1971) Simple memory: a theory for archicortex. Philos Trans R Soc Lond B 262:23–81
McNaughton B, Morris R (1987) Hippocampal synaptic enhancement and information storage within a distributed memory system. Trends Neurosci 10:408–415
Ming GI, Song H (2011) Adult neurogenesis in the mammalian brain: significant answers and significant questions. Neuron 70:687–702
Myers CE, Scharfman HE (2009) A role for hilar cells in pattern separation in the dentate gyrus: a computational approach. Hippocampus 19:321–337
Myers CE, Scharfman HE (2011) Pattern separation in the dentate gyrus: a role for the CA3 backprojection. Hippocampus 21:1190–1215
Myers CE, Bermudez-Hernandez K, Scharfman HE (2013) The influence of ectopic migration of granule cells into the hilus on dentate gyrus-CA3 function. PLoS ONE 8:e68208
Nitz D, McNaughton B (2004) Differential modulation of CA1 and dentate gyrus interneurons during exploration of novel environments. J Neurophysiol 91:863–872
O'Reilly RC, McClelland JC (1994) Hippocampal conjunctive encoding, storage, and recall: avoiding a tradeoff. Hippocampus 4:661–682
Pearson K (1895) Notes on regression and inheritance in the case of two parents. Proc R Soc Lond 58:240–242
Rolls ET (1989a) Functions of neuronal networks in the hippocampus and neocortex in memory. In: Byrne JH, Berry WO (eds) Neural models of plasticity: experimental and theoretical approaches. Academic Press, San Diego, pp 240–265
Rolls ET (1989b) The representation and storage of information in neural networks in the primate cerebral cortex and hippocampus. In: Durbin R, Miall C, Mitchison G (eds) The computing neuron. Addition-Wesley, Wokingham, pp 125–159
Rolls ET (1989c) Functions of neuronal networks in the hippocampus and cerebral cortex in memory. In: Cotterill R (ed) Models of brain function. Cambridge University Press, New York, pp 15–33
Rolls ET (2016) Pattern separation, completion, and categorization in the hippocampus and neocortex. Neurobiol Learn Mem 129:4–28
Sahay A, Wilson DA, Hen R (2011a) Pattern separation: a common function for new neurons in hippocampus and olfactory bulb. Neuron 70:582–588
Sahay A, Scobie KN, Hill AS, O'Carroll CM, Kheirbek MA, Burghardt NS, Fenton AA, Dranovsky A, Hen R (2011b) Increasing adult hippocampal neurogenesis is sufficient to improve pattern separation. Nature 472:466–470
Santoro A (2013) Reassessing pattern separation in the dentate gyrus. Front Behav Neurosci 7:96
Scharfman HE, Myers CE (2016) Corruption of the dentate gyrus by "dominant'' granule cells: implications for dentate gyrus function in health and disease. Neurobiol Learn Mem 129:69–82
Schmidt B, Marrone DF, Markus EJ (2012) Disambiguating the similar: the dentate gyrus and pattern separation. Behav Brain Res 226:56–65
Shimazaki H, Shinomoto S (2010) Kernel bandwidth optimization in spike rate estimation. J Comput Neurosci 29:171–182
Spalding KL, Bergmann O, Alkass K, Bernard S, Salehpour M, Huttner HB, Boström E, Westerlund I, Vial C, Buchholz BA, Possnert G, Mash DC, Druid H, Frisén J (2013) Dynamics of hippocampal neurogenesis in adult humans. Cell 153:1219–1227
Squire L (1987) Memory and Brain. Oxford University Press, New York
Steriade M, McCormick D, Sejnowski T (1993) Thalamocortical oscillations in the sleeping and aroused brain. Science 262:679–685
Traub RD, Whittington MA (2010) Cortical oscillations in health and diseases. Oxford University Press, New York
Treves A, Rolls ET (1991) What determines the capacity of autoassociative memories in the brain? Network 2:371–397
Treves A, Rolls ET (1992) Computational constraints suggest the need for two distinct input systems to the hippocampal CA3 network. Hippocampus 2:189–199
Treves A, Rolls ET (1994) Computational analysis of the role of the hippocampus in memory. Hippocampus 4:374–391
van Dijk MT, Fenton AA (2018) On how the dentate gyrus contributes to memory discrimination. Neuron 98:832–845
Wang XJ (2003) Neural oscillations. In: Nadel L (ed) Encyclopedia of cognitive science. MacMillan, London, pp 272–280
Wang XJ (2010) Neurophysiological and computational principles of fscortical rhythms in cognition. Physiol Rev 90:1195–1268
Wang X, Liu H, Morstein J, Novak AJE, Trauner D, Xiong Q, Yu Y, Ge S (2020) Metabolic tuning of inhibition regulates hippocampal neurogenesis in the adult brain. Proc Natl Acad Sci USA 117:25818–25829
Willshaw D, Buckingham J (1990) An assessment of Marr's theory of the hippocampus as a temporary memory store. Philos Trans R Soc Lond B 329:205–215
Yassa MA, Stark CEL (2011) Pattern separation in the hippocampus. Trends Neurosci 34:515–525
Yim MY, Hanuschkin A, Wolfart J (2015) Intrinsic rescaling of granule cells restores pattern separation ability of a dentate gyrus network model during epileptic hyperexcitability. Hippocampus 25:297–308